

## 恶劣条件下多谱段偏振目视辅助光学成像技术

付强<sup>1\*</sup>, 战俊彤<sup>1</sup>, 张肃<sup>1</sup>, 段锦<sup>1</sup>, 朱京平<sup>2</sup>, 黄丽清<sup>2</sup>, 史浩东<sup>1</sup>, 李英超<sup>1</sup>, 姜会林<sup>1,3\*\*</sup>

<sup>1</sup>长春理工大学空间光电技术研究所, 吉林 长春 130022;

<sup>2</sup>西安交通大学电信学院, 陕西 西安 710049;

<sup>3</sup>北京理工大学光电学院, 北京 100081

**摘要** 开展了多谱段信息融合的偏振成像探测方法和技术研究, 提出了多谱段偏振成像仪器总体方案; 深入分析了目标起偏和传输特性建模与测试、高消光比金属微纳格栅偏振元件的优化、多谱段偏振成像探测系统光学设计、多谱段偏振信息处理等关键技术方案。提出一种新颖的深度网络, 通过自学习策略来解决偏振图像融合问题, 为研制多谱段偏振成像探测实验样机提供技术支撑, 以满足偏振光学成像中目视辅助和引导的实际应用需求。

**关键词** 成像系统; 多谱段偏振; 目视辅助; 偏振特性; 微纳格栅

中图分类号 O439 文献标志码 A

DOI: 10.3788/AOS230961

### 1 引言

现有光电仪器大多采用单一谱段或红外多谱段探测成像技术, 存在探测距离近、去雾能力弱、识别效果差等不足, 受到大气环境, 特别是雾霾、烟尘中气溶胶的吸收和散射<sup>[1]</sup>的影响, 系统接收的能量有限, 无法实现高对比度、高分辨率的成像探测, 仅能满足特定条件下的探测需求, 却不能满足极端恶劣条件的成像需求。偏振具有“凸显目标”“穿透烟雾”“辨别真伪”的优势, 使得多谱段偏振成像成为一种适应复杂恶劣环境的新型成像探测技术<sup>[2-4]</sup>。

由于偏振光具有更好的穿透能力和更大的信息携带量, 因此基于偏振光的成像技术可以更好地解决雾霾场景图像对比度降低、颜色失真、细节信息丢失等问题。2023年, 李皓等<sup>[5]</sup>设计了基于现场图像采集的偏振信息导航传感器系统, 证明了近紫外波段偏振度图像有更好的成像效果。2022年, 王姬等<sup>[6]</sup>系统地介绍了偏振透雾成像技术的基本原理、物理模型、算法技术和成像效果, 并依据现有技术的优缺点对偏振透雾成像技术进行分析与展望。同年, 雷腾等<sup>[7]</sup>阐述了基于偏振的去散射原理以及偏振信息的作用距离, 随后介绍了基于该原理的各类偏振成像系统应用的最新进展。2017年, 曾祥伟等<sup>[8]</sup>的研究表明在近红外波段和中红外波段, 圆偏振成像技术可以提升红外系统的透雾性能。2016年, 夏璞等<sup>[9]</sup>设计了一种可快速去雾的偏振成像系统, 且该成像系统在 2048 pixel × 2048 pixel 及 180 Hz 下可获得稳定

的彩色去雾图像。本团队对偏振光成像有一定的研究基础, 先后完成了海雾、雾霾和油雾等介质的偏振成像研究<sup>[10-14]</sup>。

本团队提出了多谱段偏振成像仪器的总体设计方案, 通过对微纳格栅的分焦平面偏振器件的周期、光学厚度和占空比进行选择, 对多光路成像光学系统进行设计, 实现了多谱段高质量偏振成像仪器系统集成。针对传统的基于深度学习的图像处理技术不能解决偏振图像融合的问题, 利用新型的深度网络, 通过自学习策略来融合偏振图像。利用目标与背景偏振差异特性以及红外辐射特性, 实现图像去雾增强和目标分类识别, 以改善成像目视效果。

### 2 恶劣环境下目标偏振传输特性理论与模型

目前, 国外典型的多谱段偏振成像仪器如表1所示, 国内典型的多谱段偏振成像仪器如表2所示。目前对于偏振仪器的研制已经向实时性、小型化, 以及多维信息探测发展, 基于微纳格栅的分焦平面型偏振仪器为偏振探测的研究提供了新的器件, 在探测的实时性及结构的简化性上具有显著的优势, 但受到工艺的限制, 目前只能实现线偏振的探测, 且消光比较低, 不能获得满意的成像效果。偏振微纳阵列器件如能在结构设计和工艺实现上取得突破, 将具有良好的应用前景, 并产生巨大的经济效益。

针对探测目标状态不同、辐射光谱不同、尺寸形状

收稿日期: 2023-05-10; 修回日期: 2023-06-18; 录用日期: 2023-07-31; 网络首发日期: 2023-08-04

基金项目: 国家自然科学基金(62127813, 61890963)、吉林省教育厅项目(JJKH20220744KJ)

通信作者: \*fuqiang@cust.edu.cn; \*\*hljiang@bit.edu.cn

表1 国外典型的多谱段偏振成像仪器  
Table 1 Typical multispectral polarization imaging instruments in foreign countries

Type	Working principle	Time	Unit	Spectral range / $\mu\text{m}$	Polarization component
Rotating polarizer type	Select different polarizer sequences using motor rotation	2001	U. S. Air Force Laboratory	0.4–0.8	3
Sound and light adjustable filter type <sup>[15–16]</sup>	AOTF $\pm 1$ level diffraction polarization spectroscopy	2014	U. S. Army Laboratory	1.0–1.6	4
Liquid crystal type	Bit phase modulation (LCVR) or spectroscopy (LCTF) via liquid crystal	2018	Polaris Sensor Technologies, Inc.	1.5–1.8	3
Split amplitude type	Dividing the incident light path into four beams, multiple CCD detection	2007	Bulgarian Academy of Sciences	0.52–0.75	4
Grating dispersion type	According to the grating anisotropic polarization spectroscopy characteristics, the separation of $\pm 1$ level diffracted light in S3	2010	University of Northern California, USA	0.5–0.7	4
Channel modulation type	Modulate the polarization information to different channels and reconstruct the polarization information by demodulation	2014	University of Arizona, USA	0.4–0.85	4
Split-aperture type	Split-aperture type optical imaging system with polarization modulation of different areas of the aperture	2020	Fuji Film Corporation, Japan	0.47–0.84	3
Bifocal plane type	Micro and nano wire grid arrays	2016	Japan SONY Corporation	0.4–0.7	3

表2 国内典型的多谱段偏振成像仪器  
Table 2 Typical multispectral polarization imaging instruments in China

Type	Working principle	Time	Unit	Spectral range / $\mu\text{m}$	Polarization component
Sound and light adjustable filter type	AOTF $\pm 1$ level diffraction polarization spectroscopy	2018	Army Artillery and Air Defense Academy <sup>[17]</sup>	0.45–0.95	3
Liquid crystal type	Bit phase modulation (LCVR) or spectroscopy (LCTF) via liquid crystal	2016	Northwestern Polytechnic University	0.4–1	3
Split amplitude type	Dividing the incident light path into four beams, multiple CCD detection	2015	Northwestern Polytechnic University	0.45–0.7	3
Grating dispersion type	According to the grating anisotropic polarization spectroscopy characteristics, the separation of $\pm 1$ level diffracted light in S3	2017	Lanzhou Institute of Space Technology	0.4–1.0	3
Channel modulation type	Modulate the polarization information to different channels and reconstruct the polarization information by demodulation	2017	Nanjing University of Science and Technology	0.45–0.7	3
Split-aperture type	Split-aperture optical imaging system for different areas of the aperture	2017	Xi'an Institute of Optics and Mechanics, Chinese Academy of Sciences	0.4–0.75	4
Bifocal plane type	Perform polarization modulation	2021	Huazhong University of Science and Technology	0.532, 0.81, 1.55	4

不同、烟尘雾霾传输环境复杂、光场干扰多变等因素导致偏振特性产生差异的问题,构建目标多谱段起偏模

型与偏振特性传输模型,揭示典型目标多谱段起偏规律和雾霾烟尘天气多谱段偏振传输规律,为多谱段偏

振信息处理提供理论依据。

在大气偏振传输和辐射传输理论的基础上,研究典型复杂天候环境下偏振、微光多模态信息的特性传输相关基础理论及描述方法,分析光在雾霾、沙尘、烟雾等恶劣天气下的偏振光传输特性,建立偏振光在雾霾、沙尘、烟雾粒子下的散射模型,同时建立以环境参数为变量,以偏振、能量特性变化为输出的传输模型<sup>[18-22]</sup>,通过开展室内测试和外场实验测试进行验证。

开展了复杂环境全偏振成像技术基础问题的研究和基于Mie散射的蒙特卡罗偏振传输模型的研究,建立了球形粒子环境对偏振特性影响的数学模型<sup>[23-24]</sup>。在此基础上,对非球形粒子在不同参数下的传输特性进行仿真<sup>[25]</sup>,为恶劣条件下非球形随机取向粒子群偏

振传输特性研究提供参考。

入射光束与散射光束的斯托克斯矢量之间的关系可由散射介质的穆勒矩阵 $M$ 表示:

$$M = \begin{bmatrix} m_{11} & m_{12} & m_{13} & m_{14} \\ m_{21} & m_{22} & m_{23} & m_{24} \\ m_{31} & m_{32} & m_{33} & m_{34} \\ m_{41} & m_{42} & m_{43} & m_{44} \end{bmatrix} \quad (1)$$

当入射光经过散射介质后,其原始的偏振态发生退偏,出射光的偏振矢量 $S'$ 可以通过穆勒矩阵与入射光的斯托克斯矢量 $S$ 相乘得到,其表达式为

$$S' = M'(\theta, \phi)S, \quad (2)$$

式中: $M'(\theta, \phi) = R(-\phi)M(\theta)R(-\theta)$ , $R(-\theta)$ 为光相对于参考面与散射面的斯托克斯矢量之间转换的旋转矩阵; $\theta$ 和 $\phi$ 分别为散射角和方位角。

$$\begin{aligned} R(-\phi)M(\theta)R(-\theta) &= \\ \begin{bmatrix} 1 & 0 & 0 & 0 \\ 0 & \cos(2\phi) & -\sin(2\phi) & 0 \\ 0 & \sin(2\phi) & \cos(2\phi) & 0 \\ 0 & 0 & 0 & 1 \end{bmatrix} &\begin{bmatrix} S_{11}(\theta) & S_{12}(\theta) & 0 & 0 \\ S_{21}(\theta) & S_{11}(\theta) & 0 & 0 \\ 0 & 0 & S_{33}(\theta) & S_{34}(\theta) \\ 0 & 0 & -S_{34}(\theta) & S_{33}(\theta) \end{bmatrix} &\begin{bmatrix} 1 & 0 & 0 & 0 \\ 0 & \cos(2\phi) & -\sin(2\phi) & 0 \\ 0 & \sin(2\phi) & \cos(2\phi) & 0 \\ 0 & 0 & 0 & 1 \end{bmatrix} = \\ \begin{bmatrix} S_{11}(\theta) & S_{12}(\theta) & 0 & 0 \\ S_{12}(\theta)\cos(2\phi) & S_{11}(\theta)\cos(2\phi) & -S_{33}(\theta)\sin(2\phi) & -S_{33}(\theta)\sin(2\phi) \\ S_{12}(\theta)\cos(2\phi) & S_{11}(\theta)\sin(2\phi) & S_{33}(\theta)\cos(2\phi) & S_{33}(\theta)\cos(2\phi) \\ 0 & 0 & -S_{34}(\theta) & S_{33}(\theta) \end{bmatrix} &= \\ \begin{bmatrix} S_{11}(\theta) & S_{12}(\theta)\cos(2\phi) & -S_{12}(\theta)\cos(2\phi) & 0 \\ S_{12}(\theta)\cos(2\phi) & S_{11}(\theta)\cos^2(2\phi) - S_{33}(\theta)\sin^2(2\phi) & -[S_{11}(\theta) + S_{33}(\theta)]\sin(2\phi)\cos(2\phi) & -S_{34}(\theta)\sin(2\phi) \\ S_{12}(\theta)\sin(2\phi) & [S_{11}(\theta) + S_{33}(\theta)]\sin(2\phi)\cos(2\phi) & S_{33}\cos^2(2\phi) - S_{11}(\theta)\sin^2(2\theta) & S_{34}(\theta)\cos(2\phi) \\ 0 & -S_{34}(\theta)\sin(2\phi) & -S_{34}(\theta)\cos(2\phi) & S_{33}(\theta) \end{bmatrix}, & (3) \end{aligned}$$

得到的各参量分别为

$$m_{11} = S_{11}, m_{12} = m_{21} = m_{12}\cos(2\phi), \quad (4)$$

$$m_{13} = -m_{31} = -S_{12}(\theta)\sin(2\phi) = S_{12}\cos\left[2\left(\phi + \frac{\pi}{4}\right)\right] = m_{12}\left(\phi + \frac{\pi}{4}\right), \quad (5)$$

$$m_{14} = m_{41} = 0, m_{22} = S_{11}(\theta)\cos^2(2\phi) - S_{33}(\theta)\sin^2(2\phi) = \frac{m_{11} - m_{33}}{2} + \frac{m_{11} + m_{33}}{2}\cos(4\phi), \quad (6)$$

$$m_{23} = -m_{32} = -S_{11}\cos(2\phi)\sin(2\phi) - S_{33}\sin(2\phi)\cos(2\phi) = -\frac{m_{11} + m_{33}}{2}\sin(4\phi), \quad (7)$$

$$m_{33} = -S_{11}\left(\phi \pm \frac{\pi}{4}\right), m_{24} = -m_{34}\sin(2\phi), m_{34} = S_{34}\cos(2\phi) = m_{24}\left(\phi - \frac{\pi}{4}\right). \quad (8)$$

由上述矩阵之间的关系可知,在中间传递过程中,穆勒矩阵中的16个元素具有以下关系:

1) $m_{12} = m_{21}$ , $m_{13}$ 相对于 $m_{12}$ 的图样不变,但是转过 $45^\circ$ ,且 $m_{13} = -m_{31}$ ;

2) $m_{14} = m_{41} = 0$ , $m_{33} = -m_{22}$ ,且转过 $-45^\circ$ ;

3) $m_{23} = -m_{32}$ , $m_{24} = m_{42}$ ;

4) $m_{34} = -m_{43}$ ,且相对于 $m_{24}$ 转过 $-45^\circ$ 。

假设入射光束的斯托克斯矢量分别选用

$$S_1 = [1, 0, 0, 0]^T, \quad S_2 = [1, 1, 0, 0]^T, \quad S_3 = [1, 0, 1, 0]^T, \quad S_4 = [1, 0, 0, 1]^T, \quad (9)$$

当选择  $S_1$  光束作为入射光时,有

$$[m_1^{(1)}, m_2^{(1)}, m_3^{(1)}, m_4^{(1)}]^T = \mathbf{M} \cdot \mathbf{S}_1 = [m_{11}, m_{21}, m_{31}, m_{41}]^T。 \quad (10)$$

通过式(10)统计4种不同类型偏振光的散射矩阵,就可以获得散射图像矩阵第一列的4幅图像。当另外3种光入射时,有

$$\begin{cases} [m_1^{(2)}, m_2^{(2)}, m_3^{(2)}, m_4^{(2)}]^T = \mathbf{M} \cdot \mathbf{S}_2 = [m_{11} + m_{12}, m_{21} + m_{22}, m_{31} + m_{32}, m_{41} + m_{42}]^T \\ [m_1^{(3)}, m_2^{(3)}, m_3^{(3)}, m_4^{(3)}]^T = \mathbf{M} \cdot \mathbf{S}_3 = [m_{11} + m_{13}, m_{21} + m_{23}, m_{31} + m_{33}, m_{41} + m_{43}]^T \\ [m_1^{(4)}, m_2^{(4)}, m_3^{(4)}, m_4^{(4)}]^T = \mathbf{M} \cdot \mathbf{S}_4 = [m_{11} + m_{14}, m_{21} + m_{24}, m_{31} + m_{34}, m_{41} + m_{44}]^T \end{cases} \quad (11)$$

通过式(10)、(11)可求得其余元素,并采用蒙特卡罗方法,当入射光束为以上4种光时,分别统计散射后的光子斯托克斯矢量,再通过MATLAB软件仿真就可以得到理论上的强度图像。

建立以3种激光波长(450、532、671 nm)的6种偏振光( $0^\circ$ 、 $45^\circ$ 、 $90^\circ$ 、 $135^\circ$ 线偏光,左旋、右旋圆偏振光)为

输入,以介质粒子湿度与介质颗粒浓度为变量,以偏振光传输特性改变量为输出的数学模型<sup>[26]</sup>,深入分析浑浊介质下的偏振传输规律。**图1**为蒙特卡罗偏振传输仿真软件演示界面,**图2**为穆勒矩阵的实测结果。可以看到,实测的和仿真的穆勒矩阵图形对称情况基本相似,且它们的变化规律和模拟结果有很好的一致性。

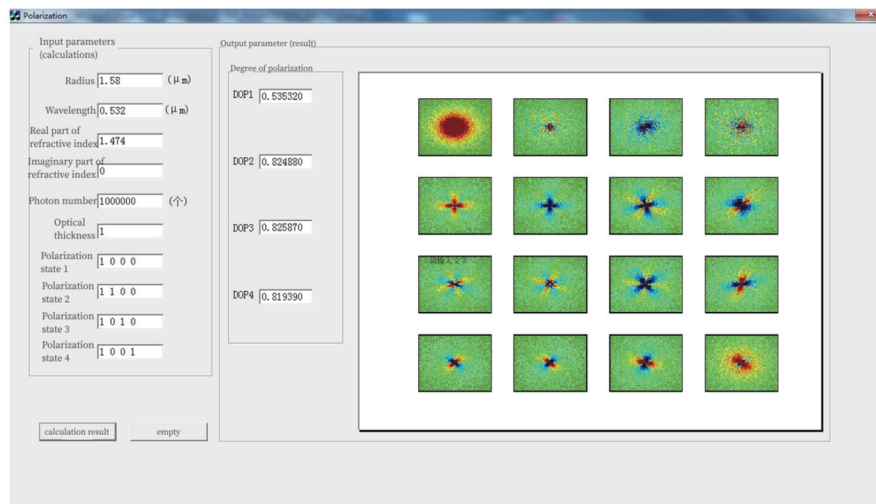


图1 蒙特卡罗偏振传输仿真软件演示界面

Fig. 1 Demonstration interface in the Monte Carlo polarization transmission simulation software

为了探究大气、烟雾等环境下光传输偏振特性,建立了室内大气湍流模拟装置、烟雾环境模拟装置、海水模拟装置等实验平台,并在室内及外场进行了偏振光传输实验。**图3**所示为大气湍流模拟装置、烟雾环境模拟装置、海水环境模拟装置。利用烟雾环境模拟装置开展了偏振光传输特性测试实验,建立了激光传输偏振特性测试实验系统,如**图4**所示,并在球形粒子模拟环境下进行了不同波长、不同初始状态的偏振光传输特性测试。

### 3 微纳格栅的分焦平面偏振信息获取技术

本文提出一种微纳格栅偏振片阵列的优化设计方法,以解决目前分焦平面偏振成像器件只有微纳线格栅而不能产生圆偏振光的缺陷,并提出新的手性微纳圆形格栅机理;分析分焦平面偏振成像消光比低的物理本质、线形格栅产生高消光比的物理机理,以及制备参数偏差对消光比的影响规律。将微纳线格栅和圆格线结合,探

索制备全偏振高消光比分焦平面成像新器件,为多谱段多维度偏振高分辨成像探测仪器研制提供参考。

根据微偏振片阵列制作工艺的不同,可将微偏振成像技术大致为三类:基于含碘化物聚乙烯醇(PVA)薄膜的技术;基于液晶材料的技术;基于金属微纳光栅的技术。比较3种技术的优缺点,发现基于金属微纳光栅的方法的像素间串扰最小,而且偏振性能最稳定,偏振效果最好,因此选用基于金属微纳光栅的制作方式。除了制造工艺会影响微偏振片阵列的性能,微偏振片阵列的各设计参数也会影响微偏振片阵列的性能,从而影响成像质量。

在设计光栅阵列的基底材料、栅槽深度、光栅周期、光栅深度等相关参数时,使用光栅衍射理论和等效介质理论进行分析。利用电矢量垂直于光栅刻槽(TM)时的偏振透射率( $T_{TM}$ )和电矢量平行于光栅刻槽(TE)时的偏振透射率( $T_{TE}$ )来分析基底折射率对于光栅透射率和消光比的影响。

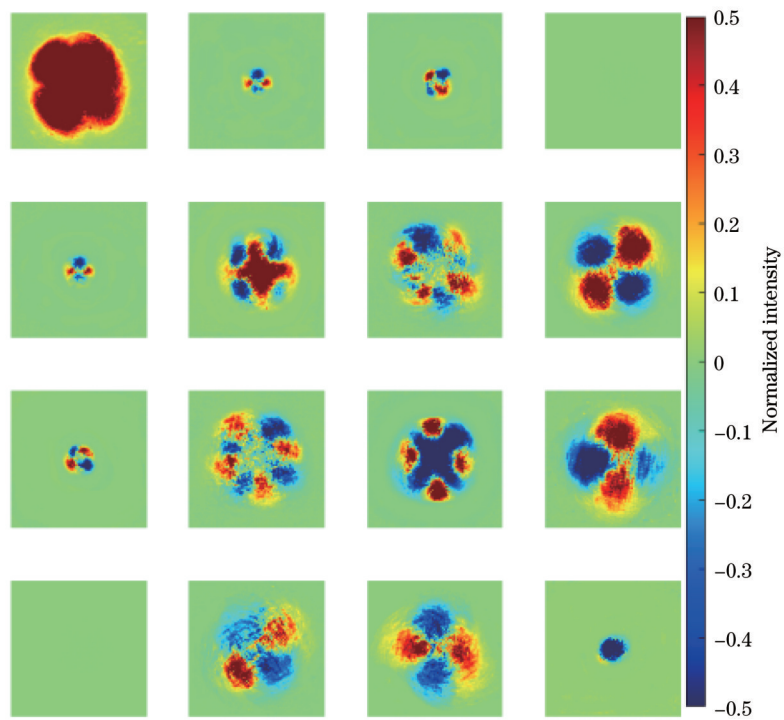


图2 穆勒矩阵实测图像

Fig. 2 Measured images of Muller's matrix



图3 环境模拟装置。(a)大气湍流模拟装置;(b)烟雾环境模拟装置;(c)海水环境模拟装置

Fig. 3 Environmental simulation device. (a) Atmosphere turbulence simulation device; (b) smog simulation device; (c) seawater simulation device

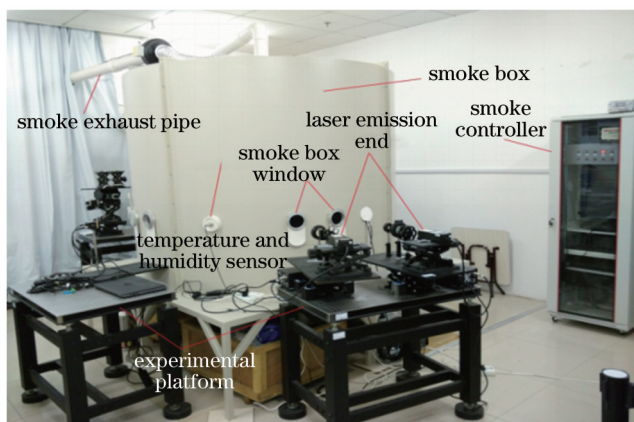


图4 激光传输实验设备

Fig. 4 Laser transmission experiment equipment

$$T_{\text{TM}} = \frac{4nA^2}{1 + (1 + n)^2 A^2}, \quad (12)$$

$$T_{\text{TE}} = \frac{4nB^2}{1 + (1 + n)^2 B^2}, \quad (13)$$

$$\begin{aligned} \frac{1}{A} = \frac{4P}{\lambda} & \left\{ \ln \left[ \csc \frac{\pi(T-a)}{2P} \right] + \right. \\ & \left. \frac{Q \cos^4 [\pi(P-a)/(2P)]}{1 + Q \sin^4 [\pi(P-a)/(2a)]} + \frac{1}{16} \left( \frac{P}{\lambda} \right)^2 \left[ 1 - \right. \right. \\ & \left. \left. 3 \sin^2 \frac{\pi(P-a)}{2P} \right]^2 \cos^4 \frac{\pi(P-a)}{2P} \right\}, \quad (14) \end{aligned}$$

$$\begin{aligned} B = & \left\{ \ln \left[ \csc \frac{\pi a}{2P} \right] + \frac{Q \cos^4 [\pi a/(2P)]}{1 + Q \sin^4 [\pi a/(2P)]} + \right. \\ & \left. \frac{1}{16} \left( \frac{P}{\lambda} \right)^2 \left[ 1 - 3 \sin^2 \frac{\pi a}{2P} \right]^2 \cos^4 \frac{\pi a}{2P} \right\}, \quad (15) \end{aligned}$$

式中： $n$  为透明基底材料的折射率； $Q =$

$$\frac{1}{[1 - (P/\lambda)^2]^{1/2}} - 1, P \text{ 为光栅周期; } a \text{ 为光栅宽度; } \lambda \text{ 为入射光波长。}$$

通过对金属光栅各几何参数(金属光栅深度、占空比、周期)的调节,仿真得到一维亚波长金属光栅对线偏振光透射谱的调控结果。如图5(a)所示,减小微纳线格栅周期,会显著提升抑制TE光透过的效果,并使TM透射谱段蓝移,故优化参数时可适当地减小光栅周期。但在实际制备过程中,光栅周期过小对制备工艺的要求变高,制造成本上升。在权衡性能和工艺两方面的因素后,选定200 nm周期的光栅结构作为后续

参数调控的对象。如图5(b)所示,随着光栅厚度的减小,抑制TE光透过的效果降低,TM透过率下降且其透射谱带蓝移。经综合考虑,选定厚度为150 nm的光栅作为后续参数调控的对象。如图5(c)所示,降低占空比f可使TM透射谱段显著蓝移,并提升TM透射峰的峰值和半峰全宽,但同时会减弱抑制TE透过的效果。综合考虑以上结果,选定0.5占空比为优化的占空比。需要注意的是,当周期为200 nm、光栅厚度为150 nm、占空比为0.5时,亚波长金属光栅在很宽的入射角下仍能保持较好的偏振选择特性,其透射光谱的角度变化特性如图5(d)所示。

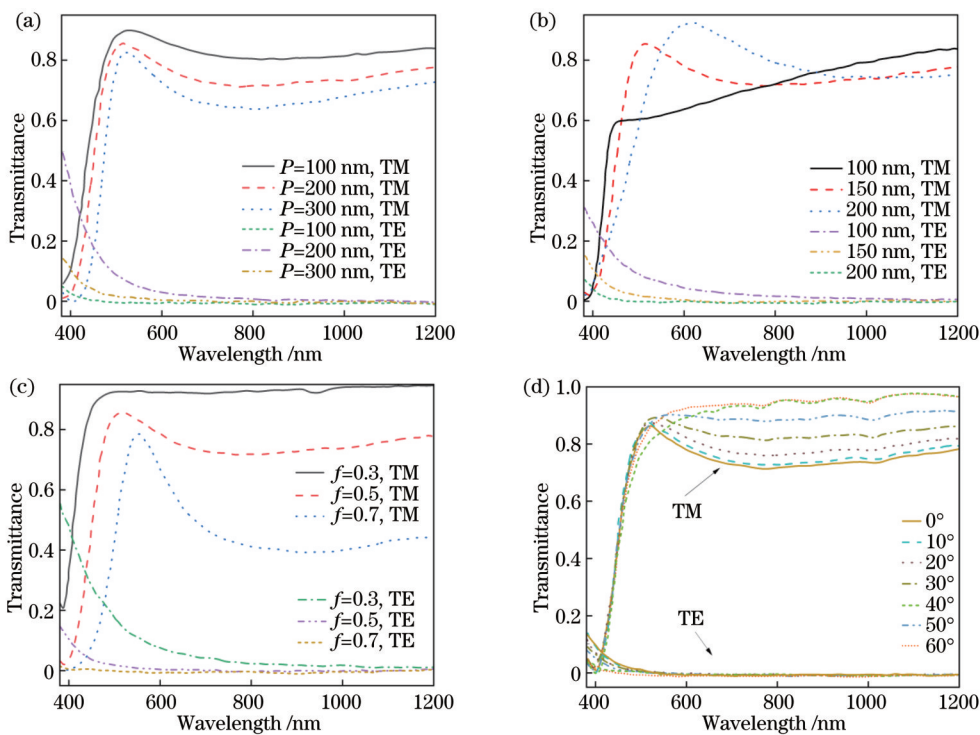


图5 微纳线格栅偏振选择性透射光谱的调控特性。(a)周期调控特性;(b)光栅厚度调控特性;(c)占空比调控特性;(d)角度调控特性  
Fig. 5 Regulation characteristics of polarization selective transmission spectra of micro/nano line grids. (a) Periodic modulation characteristics; (b) grid thickness modulation characteristics; (c) duty cycle regulation characteristics; (d) angle regulation characteristics

综上所述,当微纳线格栅的周期为200 nm、光栅厚度为150 nm、占空比为0.5时,其偏振选择特性具有高消光比、宽谱段(可见-红外)、宽入射角度、高效率等特点,基本满足可见及短波红外光选择性偏振透射特性的需求。

通过优化制备工艺参数,得到与设计预期一致的微偏振片阵列。所制备的微偏振片阵列的扫描电子显微镜(SEM)图像如图6所示。4个不同偏振方向的像素反射光强出现明显的变化,符合预期,像素间有1 μm宽的框架结构作为挡光区,用以避免像素间的信号串扰。

#### 4 多谱段全偏振成像探测系统设计及优化

针对现有仪器在雾霾烟尘条件下探测距离近、探

测灵敏度低、环境适用范围窄等问题,设计出多谱段偏振高分辨成像探测仪器;针对偏振成像光能损失大的问题,提出多光路成像光学系统设计方案。所设计的光学器件可突破基于偏振像差校正的光学系统设计、多谱段偏振定标等技术难题,实现系统仪器在烟尘、雾霾环境下成像探测能力的大幅度提升。

##### 4.1 多谱段偏振成像探测系统

多谱段偏振成像仪器由可见光/短波红外变焦光学系统、分光组件、可见光成像单元、短波红外成像单元、长波红外成像单元、图像采集控制子系统、图像处理子系统7个部分组成<sup>[18-21]</sup>。总体结构组成如图7所示,仪器外形示意图如图8所示。

可见光波段是最常用的探测波段,偏振探测中也最常使用可见光波段,其可直接显示探测目标,且目标

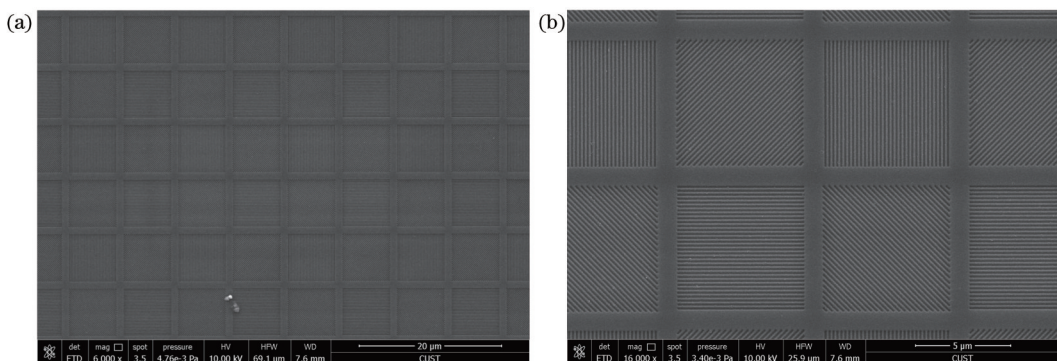


图6 微偏振片阵列的SEM图像。(a)全局图像;(b)局部放大图像  
Fig. 6 SEM images of micro-polarizer arrays. (a) Global image; (b) localized enlargement image

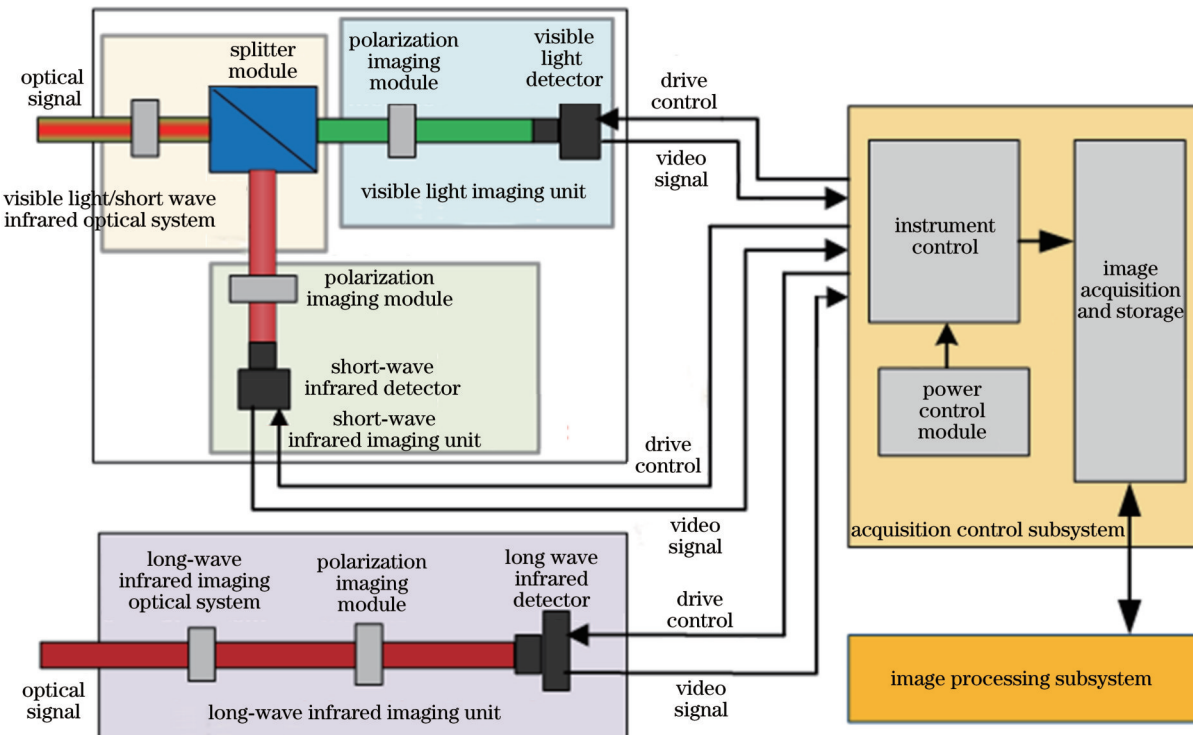


图7 总体结构组成图  
Fig. 7 Overall structure composition diagram

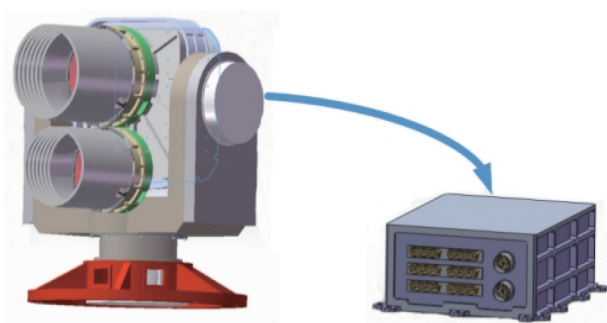


图8 总体外形示意图  
Fig. 8 Overall outline diagram

的几何形状逼真,立体感强,分辨率较高,使目标能被较好识别。可见光波段在偏振探测中的缺点是夜间照

相侦察比较困难,受天气影响比较大,在云和雾中的侦察效果不好。

短波红外对目标的识别度高,全天候适应性强,微光夜视能力强,且在大气中的传播效果较好,可以穿透一定的云层、烟雾和雨雪等,适用于远距离探测。短波红外技术可以在较低照明度的条件下成像,有助于在暗夜或低光条件下探测目标,这弥补了恶劣环境下可见光波段的不足。遗憾的是,短波红外技术无法接收物体本身发出的红外辐射,在一些特殊的恶劣环境下,其探测效果会受到影响。

长波红外成像通过检测物体本身发出的红外辐射进行成像,物体的温度越高,其红外辐射能量越大,长波红外成像即通过接收的红外线能量来获得物体表面

的温度分布。长波红外成像还具有隐蔽性好、不受电磁干扰、能远距离跟踪目标,且24小时全天候监控的特点,非常适于探测目标的热量和表面温度分布。长波红外成像系统不需要额外的照明光源,可以在完全黑暗的环境中进行探测和成像,可以提供大范围、高分辨率的热图,在温度分布分析、热障检测、能量泄漏抑制等方面具有重要应用。但是,其图像的对比度低,分辨细节能力较差,需要与可见光和短波红外配合使用。

综上所述:可见光/短波红外变焦光学系统用于收集目标的可见光与短波红外辐射;分光组件用于对可见光与短波红外两路光进行分光;可见光偏振成像单元由可见光偏振成像光学组件和可见光探测器组成;短波红外偏振成像单元由短波红外偏振成像光学组件和短波红外探测器组成;长波红外偏振成像单元由长

波红外成像光学系统、偏振成像光学组件、长波红外探测器组成。3个成像单元用于获取不同谱段的偏振图像。图像采集控制子系统完成设备驱动、仪器控制、采集时统控制、图像存储以及输入输出接口管理等功能;图像处理子系统完成对多谱段偏振信息的处理工作。

#### 4.2 系统光路设计结果与优化结果

圆偏振光具有更强的穿透烟雾的能力,因此本研究使用圆偏振光对目标进行多谱段全偏振成像,可以提升穿透效果、凸显目标。设计了多光路成像光学系统,实现了多谱段高质量偏振成像仪器系统集成。可见光偏振、短波红外偏振、长波红外偏振光学系统采用连续变焦方式<sup>[27]</sup>,从而实现大视场发现目标和长焦距详查目标,其变焦倍率为5×,具体的光学系统设计指标参数如表3所示。

表3 可见光、短波红外、长波红外偏振成像系统的指标

Table 3 Indicators of visible light, short-wave infrared, and long-wave infrared polarization imaging systems

System	Visible light system	Short-wave infrared system	Long-wave infrared system
Operating wavelength / $\mu\text{m}$	0.45–0.78	0.9–1.7	8–12
Detector size / $\mu\text{m}$	3.45	20	17
Detector resolution /(pixel $\times$ pixel)	2048 $\times$ 2048	640 $\times$ 512	640 $\times$ 512
Focal length /mm	18–90	18–90	300
F-number	2.8–5.6	2.8–5.6	1.2

一般光学系统有透射式、反射式和折反射式3种结构。透射式结构的优点是无中心遮拦、视场角大、易消除杂散光。由于所设计系统的口径较小,采用反射式结构时加工难度较大,因此选用透射式结构<sup>[28]</sup>。采用消色差方法对玻璃进行设计,通过将多种玻璃进行

组合,消除初级和高级色差<sup>[29–32]</sup>,达到各波长像质一致的目的。镜片材料无放射性,酸碱潮解度均不低于3级。可见光光学系统、短波红外光学系统、长波红外光学系统的二维结构图如图9~11所示,其中 $d_{\text{EFL}}$ 为有效焦距。

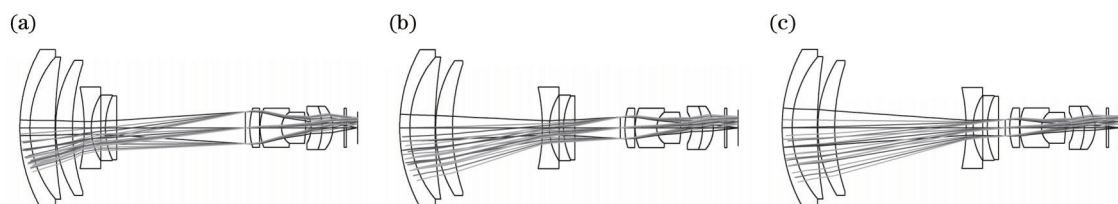


图9 可见光光学系统的二维结构。(a)  $d_{\text{EFL}}=18 \text{ mm}, F=5.6$ ; (b)  $d_{\text{EFL}}=50 \text{ mm}, F=4.5$ ; (c)  $d_{\text{EFL}}=90 \text{ mm}, F=2.8$

Fig. 9 Two-dimensional structures of visible light optical systems. (a)  $d_{\text{EFL}}=18 \text{ mm}, F=5.6$ ; (b)  $d_{\text{EFL}}=50 \text{ mm}, F=4.5$ ; (c)  $d_{\text{EFL}}=90 \text{ mm}, F=2.8$

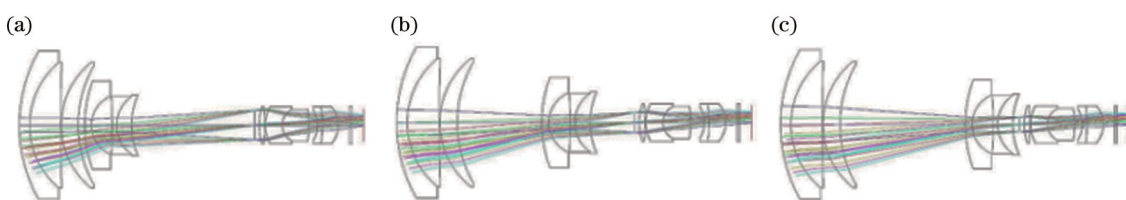


图10 短波红外光学系统的二维结构。(a)  $d_{\text{EFL}}=18 \text{ mm}, F=2.8$ ; (b)  $d_{\text{EFL}}=50 \text{ mm}, F=4.5$ ; (c)  $d_{\text{EFL}}=90 \text{ mm}, F=5.6$

Fig. 10 Two-dimensional structures of short-wave infrared optical system. (a)  $d_{\text{EFL}}=18 \text{ mm}, F=2.8$ ; (b)  $d_{\text{EFL}}=50 \text{ mm}, F=4.5$ ; (c)  $d_{\text{EFL}}=90 \text{ mm}, F=5.6$

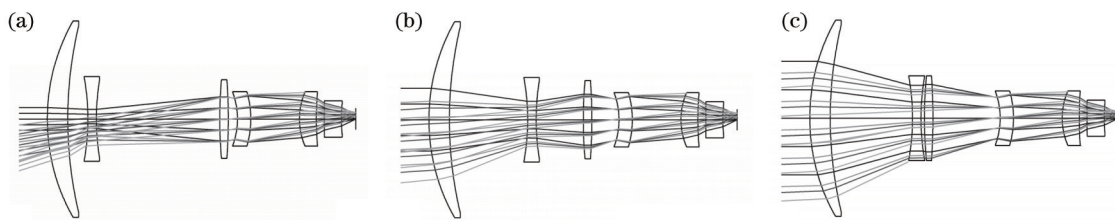
图11 长波红外光学系统的二维结构。(a) $d_{\text{EFL}}=18 \text{ mm}, F=1.2$ ;(b) $d_{\text{EFL}}=50 \text{ mm}, F=1.2$ ;(c) $d_{\text{EFL}}=90 \text{ mm}, F=1.2$ 

Fig. 11 Two-dimensional structures of long-wave infrared optical system. (a)  $d_{\text{EFL}}=18 \text{ mm}$ ,  $F=1.2$ ; (b)  $d_{\text{EFL}}=50 \text{ mm}$ ,  $F=1.2$ ; (c)  $d_{\text{EFL}}=90 \text{ mm}$ ,  $F=1.2$

可见光光学系统、短波红外光学系统、长波红外光学系统的像质如图12~14所示。可见,即使到137线对处(对应 $3.45 \mu\text{m}$ 的像元大小),各变焦位置的像

质接近,各位置MTF值大于0.05或接近0.1,中心视场在0.2~0.3,证明该系统像质较好,成像分辨率较高。

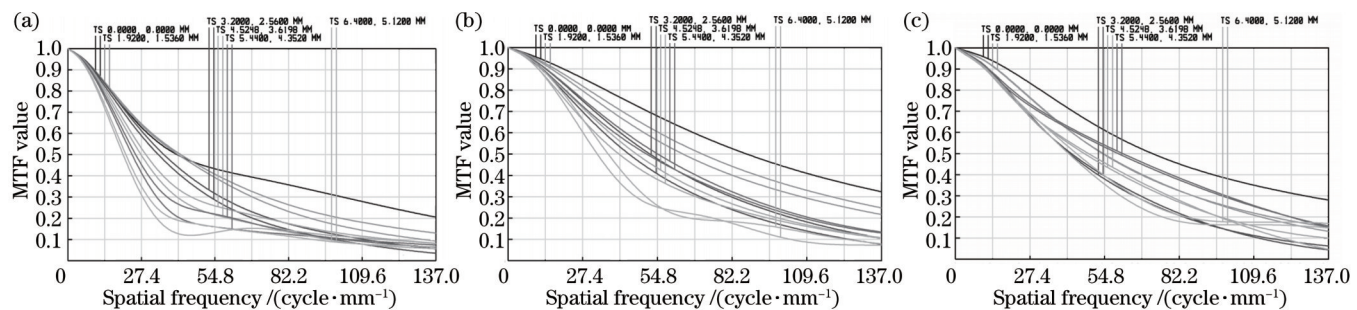
图12 不同有效焦距下可见光光学系统的MTF曲线。(a) $d_{\text{EFL}}=90 \text{ mm}$ ;(b) $d_{\text{EFL}}=50 \text{ mm}$ ;(c) $d_{\text{EFL}}=18 \text{ mm}$ 

Fig. 12 MTF curves of visible light optical systems under different effective focal length. (a)  $d_{\text{EFL}}=90 \text{ mm}$ ; (b)  $d_{\text{EFL}}=50 \text{ mm}$ ; (c)  $d_{\text{EFL}}=18 \text{ mm}$

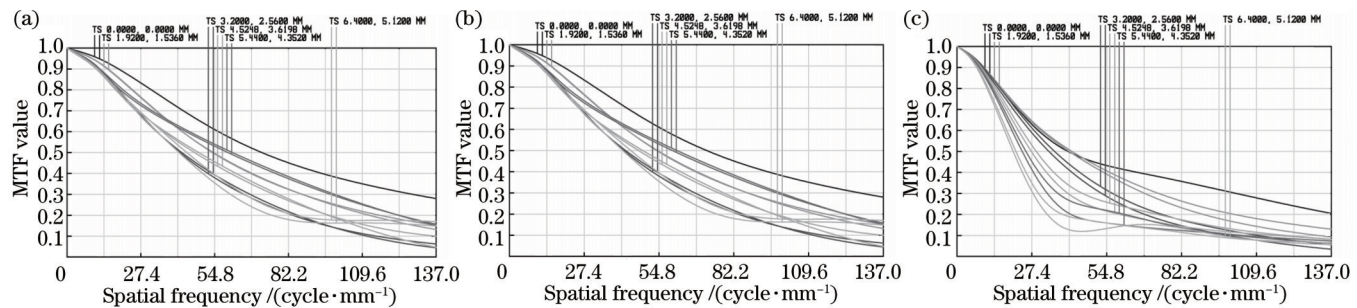
图13 不同有效焦距下短波红外光学系统的MTF曲线。(a) $d_{\text{EFL}}=18 \text{ mm}$ ;(b) $d_{\text{EFL}}=50 \text{ mm}$ ;(c) $d_{\text{EFL}}=90 \text{ mm}$ 

Fig. 13 MTF curves of short-wave infrared optical systems under different effective focal length. (a)  $d_{\text{EFL}}=18 \text{ mm}$ ; (b)  $d_{\text{EFL}}=50 \text{ mm}$ ; (c)  $d_{\text{EFL}}=90 \text{ mm}$

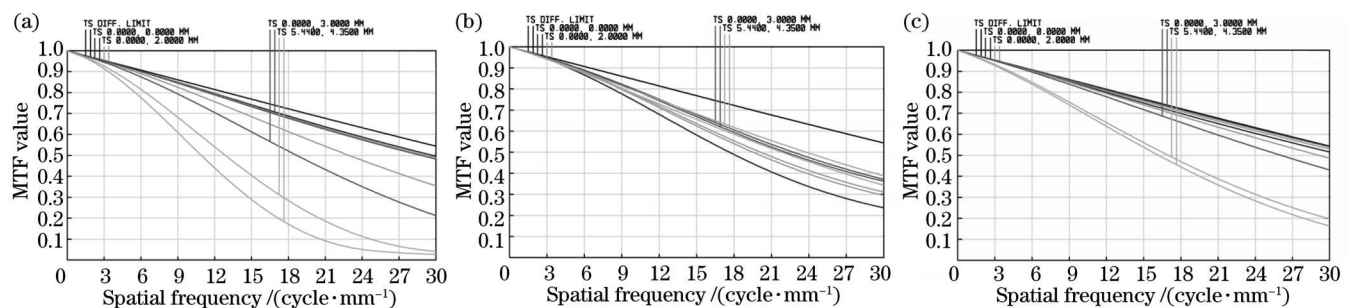
图14 不同有效焦距下长波红外光学系统的MTF曲线。(a) $d_{\text{EFL}}=18 \text{ mm}$ ;(b) $d_{\text{EFL}}=50 \text{ mm}$ ;(c) $d_{\text{EFL}}=90 \text{ mm}$ 

Fig. 14 MTF curves of long-wave infrared optical systems under different effective focal length. (a)  $d_{\text{EFL}}=18 \text{ mm}$ ; (b)  $d_{\text{EFL}}=50 \text{ mm}$ ; (c)  $d_{\text{EFL}}=90 \text{ mm}$

本文使用图像对比度作为成像质量的衡量标准,图像对比度是客观评价图像质量的重要指标,其表达式为

$$C_w = \frac{I_t - I_b}{I_b}, \quad (16)$$

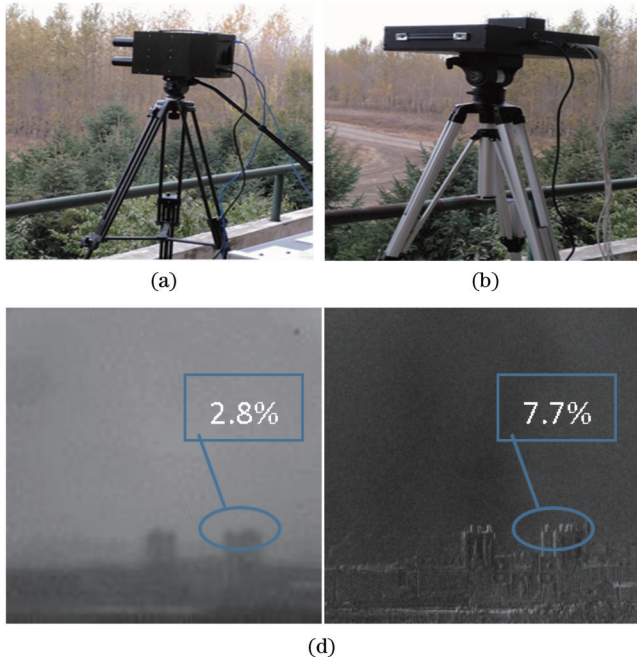


图15 雾霾环境偏振成像实验。(a)分时偏振成像装置;(b)同时偏振成像装置;(c)普通强度成像与可见光偏振成像对比;(d)普通强度成像与短波红外偏振成像对比;(e)普通强度成像与长波红外偏振成像对比

Fig. 15 Polarization imaging experiment in haze environment. (a) Time-sharing polarization imaging device; (b) simultaneous polarization imaging device; (c) normal intensity imaging versus visible light polarization imaging; (d) normal intensity imaging versus short-wave infrared polarization imaging; (e) normal intensity imaging versus long-wave infrared polarization imaging

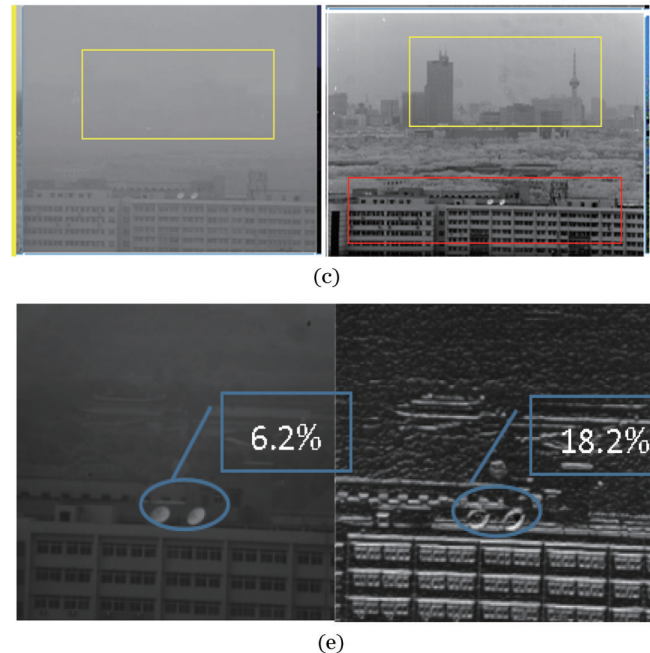
从图15可以看出,偏振可以提高图像对比度:红色区域的对比度由8.34%提高至20.07%,黄色区域的对比度由6.93%提高至22.87%,蓝色区域的对比度分别由2.8%提高至7.7%,以及由6.2%提高至18.2%。可见,所研制的偏振成像装置在复杂环境下的可见光偏振成像、短波红外偏振成像、长波红外偏振成像中均取得很好的效果,可以大幅提升成像对比度。

## 5 基于偏振特性的偏振图像处理

多谱段偏振图像经过信息融合后<sup>[26-29]</sup>,利用目标与背景偏振差异特性以及红外辐射特性<sup>[30]</sup>,实现图像去雾增强和目标分类识别,以提高成像目视效果。多源信道采集过程主要分为4个部分:图像配准与重构、多谱段图像增强与融合、基于偏振光场模型的图像去雾、基于目标偏振特性的目标分类与识别,如图16所示。

近年来,深度学习在图像融合领域得到了广泛应用,已出现多种基于深度学习的图像融合方法,例如DenseFuse、DIF-Net、U2Fusion,以及一些生成对抗网络的融合框架如FusionGAN、GANMcC。然而,这些

式中: $C_w$ 为图像对比度; $I_t$ 表示目标区域亮度; $I_b$ 为图像背景区域的整体亮度。将所设计的微偏振片阵列集成到光学系统中<sup>[33-35]</sup>,研制分时型偏振成像装置和同时型偏振成像装置,并开展了雾霾天气下被动偏振成像实验,结果如图15所示。



基于深度学习的方法都是为了融合多模态、多曝光和多聚焦图像而提出的,它们不是为极化图像融合而设计的。

本文提出一种新颖的深度网络,通过自学习策略来解决偏振图像融合问题。所提网络由编码器层、融合层和解码器层组成。对编码器提取的特征图像进行融合,再送入解码器生成融合图像<sup>[31]</sup>,给定多维偏振图像,通过从源图像中提取有效特征,从而融合构成一幅信息量丰富的偏振图像,以便后续高级图像应用。结合偏振信息的深度网络在语义分割方面的优势示例如图17所示,可以看出,融合图像的多维偏振信息量更丰富。

偏振图像融合的目的是将强度( $S_0$ )图像和线性偏振度(DoLP)图像融合为一个具有更多细节的图像。所提融合网络的整体架构如图18所示,包括编码器、融合子网和解码器三部分。将编码器提取的特征融合在一起,并经过解码器得到融合图像。所有卷积核的大小都是 $3 \times 3$ ,并使用零填充来保持特征映射大小相同。

如图18所示,编码器(encoder)将强度和DoLP图

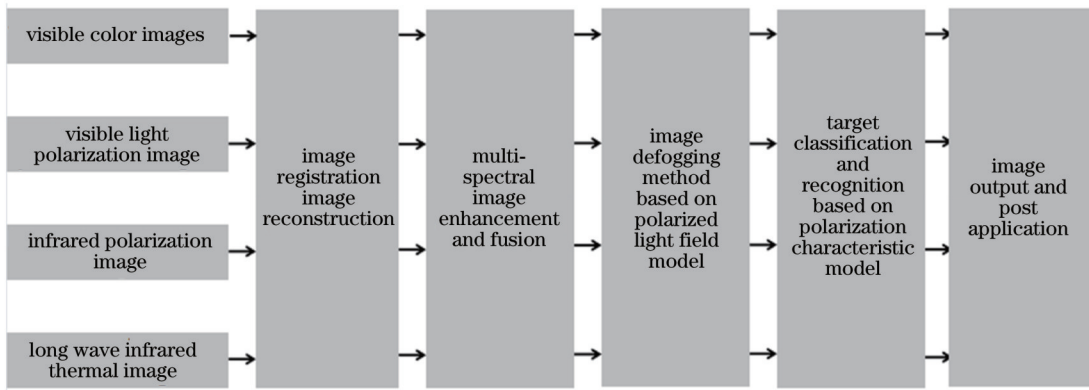


图16 信息处理分系统  
Fig. 16 Information processing subsystem

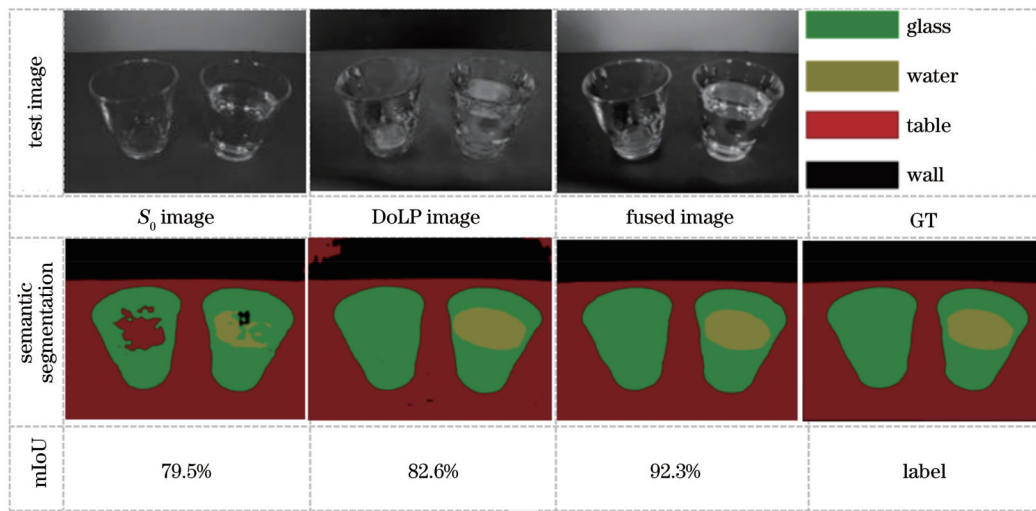


图17 多维偏振信息融合语义分割验证  
Fig. 17 Semantic segmentation verification based on multidimensional polarization information fusion

像送入具有16个输出通道的卷积层(Conv)中提取粗糙特征,然后使用ReLU激活函数进行处理。使用注意力引导密集网络(AGD)提取深度和高维特征。在AGD中使用3个卷积层(有16个输出通道),每个层后面都有一个ReLU。AGD的输出大小为 $M \times N \times 64$ ,其中 $M, N, 64$ 分别为特征映射的宽度、高度和通道数量。将从强度和DoLP图像中提取的特征映射记为 $F_{S_0}$ 和 $F_{\text{DoLP}}$ 。分别将每个通道的 $F_{S_0}$ 和 $F_{\text{DoLP}}$ 送入融合子网络(fusion sub-net),生成融合特征 $F$ ,融合任务的计算公式为

$$F_{\text{fused}}^{(i)} = F_{S_0}^{(i)} + F_{\text{DoLP}}^{(i)} + \text{Fusion}(F_{S_0}^{(i)}, F_{\text{DoLP}}^{(i)}), \quad (17)$$

式中: $\text{Fusion}(\cdot)$ 表示融合子网学习的映射函数; $i$ 表示通道数, $i \in \{1, 2, 3, \dots, 64\}$ 。

解码器(decoder)通过输出通道数分别为64、32、16、1的4个卷积层生成融合图像 $I_f$ 。除了最后一层,其余3层还使用ReLU激活函数进行处理。所提网络结构中并没有使用上采样层,这是因为该结构中采用了零填充操作。

对于图像融合问题,通常使用图像结构相似度

(SSIM)来评估融合性能,并训练网络作为损失函数。在SSIM函数的基础上,提出一种多尺度加权SSIM(MSWSSIM)损失函数,其计算公式为

$$f_{\text{loss}, 1} = 1 - \frac{1}{5} \cdot \sum_{w \in \{3, 5, 7, 9, 11\}} [\gamma_w \cdot f_{\text{loss, SSIM}}(I_{S_0}, I_f; w) + (1 - \gamma_w) \cdot f_{\text{loss, SSIM}}(I_{\text{DoLP}}, I_f; w)], \quad (18)$$

式中: $\gamma_w$ 为权重系数; $f_{\text{loss}}(x, y; w)$ 表示窗口 $w$ 内 $x$ 和 $y$ 的局部结构相似度。

$$f_{\text{loss, SSIM}}(x, y; w) = \frac{(2\bar{w}_x\bar{w}_y + C_1)(2\sigma_{w_x w_y} + C_2)}{(\bar{w}_x^2 + \bar{w}_y^2 + C_1)(\sigma_{w_x}^2 + \sigma_{w_y}^2 + C_2)}, \quad (19)$$

式中: $C_1, C_2$ 为常数; $w_x$ 表示图像 $x$ 在窗口 $w$ 内的区域;变量 $\sigma_{w_x}^2$ 和 $\sigma_{w_x w_y}$ 分别为 $w_x$ 的方差和 $w_x$ 和 $w_y$ 的协方差。

特征图中的每个像素在本质上是一个64维向量,所使用的 $F_{\text{fused}}$ 和 $F_f$ 的每个像素可以分别表示为 $g_{i,j}$ 和 $t_{i,j}$ 。由于 $g_{i,j}$ 和 $t_{i,j}$ 是高维向量,本文采用调整余弦相似度(ACOS)来计算差值:

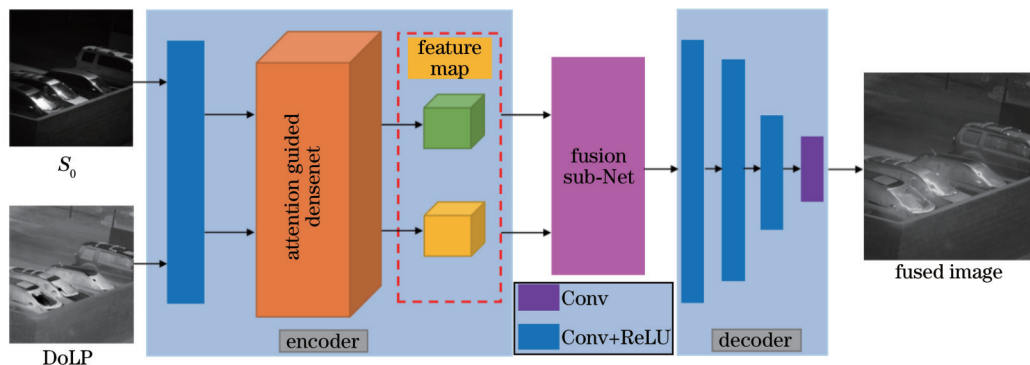


图18 偏振图像融合网络架构

Fig. 18 Polarization image fusion network architecture

$$f_{\text{loss},2} = 1 - \xi_{\text{ACOS}}(F_{\text{fused}}, F_f) = 1 - \frac{1}{M \cdot N} \sum_{i=1}^M \sum_{j=1}^N \frac{\langle \bar{g}_{i,j}, \bar{t}_{i,j} \rangle}{(\bar{g}_{i,j})_2 (\bar{t}_{i,j})_2}, \quad (20)$$

式中： $\bar{g}_{i,j}$  和  $\bar{t}_{i,j}$  表示通过减去每个维度的平均值而归一化的向量； $\xi_{\text{ACOS}}$  为图像的 ACOS。因此，最终的损失函数为

$$f_{\text{loss}} = \kappa \cdot f_{\text{loss},1} + f_{\text{loss},2}, \quad (21)$$

式中： $\kappa$  是一个平衡参数，它在实验中被设置为 0.1。

为了定性地评价本文编解码结构对于偏振图像融合的优势，将本文方法和不同融合方法的融合结果进行对比，如图 19 所示。图 19(a)展示了室内环境下手机屏幕为偏振光场景时的融合结果，可以看到，本文方法保证了目标与背景信息的充分表征，融合结果最好。图 19(b)展示了不同方法对典型的室外树木伪装场景的融合结果，可以看到，对于墙体中的伪装树木，本文方法能够实现 DoLP 和  $S_0$  图像互补信息的充分保留，而且保留了清晰的边缘和纹理。

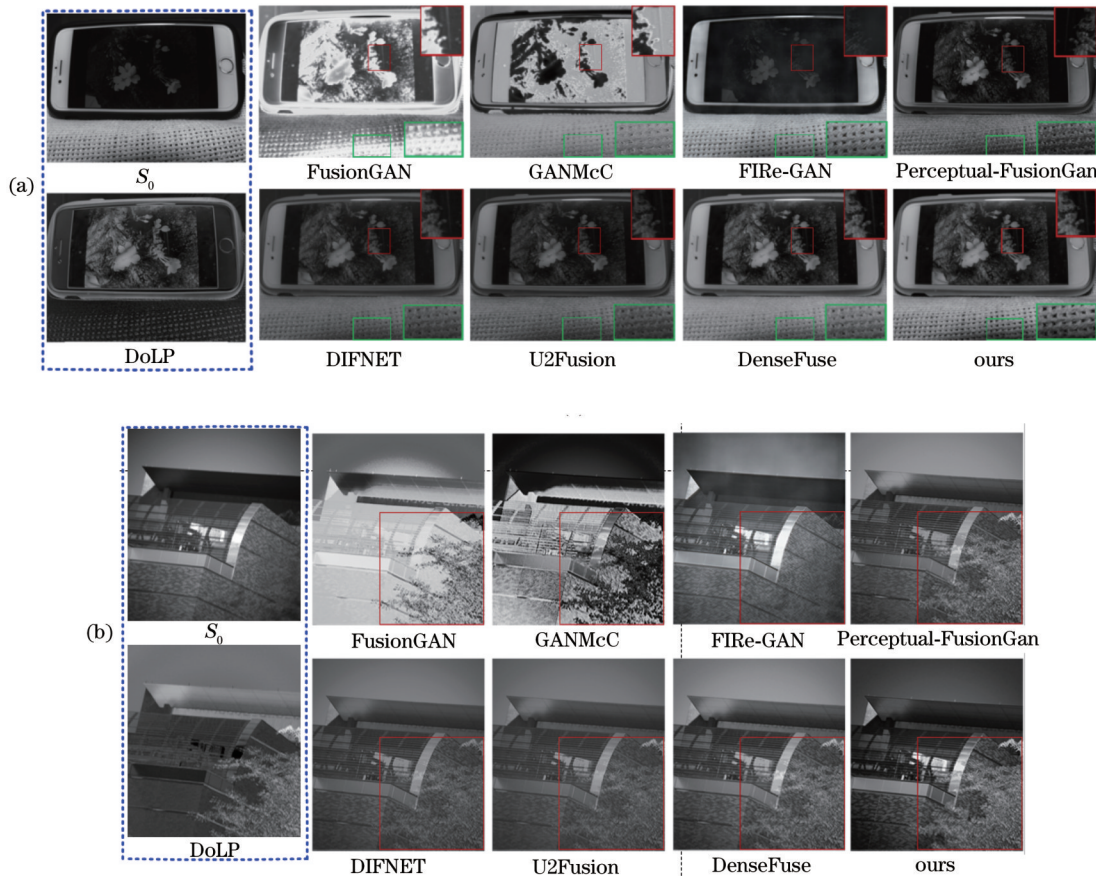


图19 不同融合方法的结果对比。(a) 手机屏幕为偏振光场景；(b) 室外树木伪装场景

Fig. 19 Comparison results of different fusion methods. (a) Mobile phone screen as polarized light scene; (b) camouflage scene of outdoor trees

## 6 结 论

针对恶劣环境和气象条件造成目标在光学探测中“认不清”“看不远”“辨不出”的问题,提出了多谱段偏振成像探测技术方案,期望在3个方面实现突破:1)在器件研制方面,改进圆形微纳格栅设计方法和微纳线栅基底材料-结构,制备高消光比分焦平面成像新器件;2)在系统设计方面,突破多光路保偏光学系统设计、高增透高保偏光学镀膜等关键技术的瓶颈,实现仪器信息获取的高时空匹配;3)在信息处理方面,研究目标偏振特性模型和偏振传输模型,改善多维信息融合、偏振去雾增强、目标分类识别等难题。

恶劣环境和天气条件不仅对光学成像探测影响极大,对飞机降落安全等的影响也极其严重。低能见度下飞机不能正常降落,造成航班停飞或延误,产生重大经济损失和社会影响。目前低能见度条件下实施进近与着陆,驾驶员大都是借助地面、机载导航设施/设备来引导飞机按照规定的航径飞向跑道,这些设备主要包括仪表着陆系统(ILS)、微波着陆系统(MLS)、卫星导航技术(GPS)、激光着陆系统、视见着陆系统。在无雷达导引或无地面指示等极端恶劣条件下,飞机无法通过上述引导方式获得有效安全的降落引导和辅助。因此,研制恶劣条件下飞机着陆目视辅助仪器具有极其重要的意义,可以提升烟雾环境、海雾环境、低照度环境等恶劣条件下飞机降落的安全性。

## 参 考 文 献

- [1] 王涵,孙晓兵,赵梅如,等.基于后验误差分析的多角度偏振成像仪气溶胶反演测试[J].光学学报,2023,43(24): 2428007.  
Wang H, Sun X B, Zhao M R, et al. Multi-angle polarization imager aerosol inversion test based on posterior error analysis[J]. Acta Optica Sinica, 2023, 43(24): 2428007.
- [2] 许珈诺,赵健,李校博,等.基于频谱信息的浑浊水下偏振成像技术[J].光学学报,2023,43(18): 1811001.  
Xu J N, Zhao J, Li X B, et al. Polarization imaging technique for turbid underwater based on spectral information[J]. Acta Optica Sinica, 2023, 43(18): 1811001.
- [3] 李岩松,赵慧洁,李娜,等.基于中红外偏振的海面太阳耀光背景下的目标探测[J].中国激光,2022,49(19): 1910004.  
Li Y S, Zhao H J, Li N, et al. Detection of marine targets covered in Sun glint based on mid-infrared polarization[J]. Chinese Journal of Lasers, 2022, 49(19): 1910004.
- [4] 孟宇飞,王晓玲,刘畅,等.四分暗通道均值比较法的双角度偏振图像去雾[J].激光与光电子学进展,2022,59(4): 0411001.  
Meng Y F, Wang X L, Liu C, et al. Dehazing of dual angle polarization image based on mean comparison of quartering dark channels[J]. Laser & Optoelectronics Progress, 2022, 59(4): 0411001.
- [5] 李皓,李沅,侯琪.恶劣天气下近紫外波段的偏振成像技术研究[J].计算机测量与控制,2023,31(1): 230-236.  
Li H, Li Y, Hou Q. Study on polarization imaging technology in near ultraviolet band in bad weather[J]. Computer Measurement & Control, 2023, 31(1): 230-236.
- [6] 王姬,卫毅,杨奎,等.基于散射光场偏振特性的透雾霾成像技术发展及展望[J].光电技术应用,2022,37(5): 20-32, 81.  
Wang J, Wei Y, Yang K, et al. Development and prospect of dehazing imaging technology based on polarization characteristic of scattering light field[J]. Electro-Optic Technology Application, 2022, 37(5): 20-32, 81.
- [7] 雷腾,王世勇,马一哲,等.散射介质条件下复杂场景的偏振成像进展及展望[J].光电技术应用,2022,37(5): 70-81.  
Lei T, Wang S Y, Ma Y Z, et al. Progress and prospect of polarization imaging for complex scenes in scattering media[J]. Electro-Optic Technology Application, 2022, 37(5): 70-81.
- [8] 曾祥伟,褚金奎,康维东.红外圆偏振光透雾性能分析[J].红外与激光工程,2017,46(12): 1204002.  
Zeng X W, Chu J K, Kang W D. Analysis on fogging performance of infrared circularly polarized light[J]. Infrared and Laser Engineering, 2017, 46(12): 1204002.
- [9] 夏璞,刘学斌,闫鹏.偏振透雾成像系统的设计与实验分析[J].西安电子科技大学学报,2016,43(2): 95-101.  
Xia P, Liu X B, Yan P. Design of and experiment on the polarization dehazing imaging system[J]. Journal of Xidian University, 2016, 43(2): 95-101.
- [10] 孙昇,王超,史浩东,等.分孔径离轴同时偏振超分辨率成像光学系统像差校正[J].物理学报,2022,71(21): 214201.  
Sun S, Wang C, Shi H D, et al. Aberration correction of sub-aperture off-axis simultaneous polarization super-resolution imaging optical system[J]. Acta Physica Sinica, 2022, 71(21): 214201.
- [11] 史浩东,王稼禹,李英超,等.复杂海况下海洋生态环境多维度光学监测方法[J].光学学报,2022,42(6): 0600004.  
Shi H D, Wang J Y, Li Y C, et al. Multi-dimensional optical monitoring method of marine ecological environment under complex sea conditions[J]. Acta Optica Sinica, 2022, 42(6): 0600004.
- [12] 战俊彤,张肃,付强,等.油雾浓度对激光偏振度的影响[J].光子学报,2016,45(3): 0314006.  
Zhan J T, Zhang S, Fu Q, et al. Impact of the oil mist concentration degree of polarization of the laser[J]. Acta Photonica Sinica, 2016, 45(3): 0314006.
- [13] 战俊彤,付强,张肃,等.前向散射角度对偏振成像对比度影响的研究[J].光学学报,2015,35(7): 0711007.  
Zhan J T, Fu Q, Zhang S, et al. Research on the effects of forward scattering angle to polarization imaging contrast[J]. Acta Optica Sinica, 2015, 35(7): 0711007.
- [14] 付强,战俊彤,张肃,等.混浊介质对偏振传输特性及成像的影响[J].现代工业经济和信息化,2014,4(18): 63-64, 89.  
Fu Q, Zhan J T, Zhang S, et al. Research on mixed programming of atmospheric transmittance calculation[J]. Modern Industrial Economy and Informationization, 2014, 4 (18): 63-64, 89.
- [15] Gupta N. Acousto-optic tunable filter based visible- to near-infrared spectropolarimetric imager[J]. Optical Engineering, 2002, 41(5): 1033-1038.
- [16] Zhan J T, Bao S C, Zhang S, et al. The research of long-optical-path visible laser polarization characteristics in smoke environment[J]. Frontiers in Physics, 2022, 10: 874956.
- [17] Cheng Y, Niu W S, Liu Z L, et al. A prototype of Enhanced Synthetic Vision System using short-wave infrared[C]//2018 IEEE/AIAA 37th Digital Avionics Systems Conference (DASC), September 23-27, 2018, London, UK. New York: IEEE Press, 2018.
- [18] Zhang S, Zhan J T, Fu Q A, et al. Effects of environment variation of glycerol smoke particles on the persistence of linear and circular polarization[J]. Optics Express, 2020, 28(14): 20236-20248.
- [19] Fu Q A, Si L L, Liu J N, et al. Design and experimental study of a polarization imaging optical system for oil spills on sea surfaces[J]. Applied Optics, 2022, 61(21): 6330-6338.
- [20] Fu Q, Luo K, Song Y, et al. Study of sea fog environment

- polarization transmission characteristics[J]. Applied Sciences, 2022, 12(17):8892.
- [21] Duggin M J, Loe R S. Algorithms for target discrimination and contrast enhancement using narrowband polarimetric image data [J]. Proceedings of SPIE, 2002, 4481: 247-225.
- [22] Duggin M J, Loe R S. Calibration and exploitation of a narrowband imaging polarimeter[J]. Optical Engineering, 2002, 41(5): 1039-1047.
- [23] 张肃, 战俊彤, 付强, 等. 不同形状的非球形粒子对偏振传输特性的影响[J]. 光学学报, 2019, 39(6): 0629001.  
Zhang S, Zhan J T, Fu Q, et al. Influence of non-spherical particles with different shapes on polarization transmission characteristic[J]. Acta Optica Sinica, 2019, 39(6): 0629001.
- [24] 于婷, 战俊彤, 马莉莉, 等. 椭球形粒子浓度对激光偏振传输特性的影响[J]. 中国激光, 2019, 46(2): 0208002.  
Yu T, Zhan J T, Ma L L, et al. Effect of ellipsoidal particle concentration on laser polarization transmission characteristics [J]. Chinese Journal of Lasers, 2019, 46(2): 0208002.
- [25] Liu X E, Heifetz A, Tseng S C, et al. High-speed inline holographic stokesmeter imaging[J]. Applied Optics, 2009, 48(19): 3803-3808.
- [26] Fu Q A, Liu X W, Yang D, et al. Improvement of pBRDF model for target surface based on diffraction and transmission effects[J]. Remote Sensing, 2023, 15(14): 3481.
- [27] Todorov T, Nikolova L, Stoilov G, et al. Spectral Stokesmeter 1: implementation of the device[J]. Applied Optics, 2007, 46(27): 6662-6668.
- [28] 邢思远, 王超, 徐森, 等. 数字微镜器件超分辨率成像光学系统装调误差影响研究[J]. 中国光学, 2021, 14(5): 1194-1201.  
Xing S Y, Wang C, Xu M, et al. Influence of alignment error on DMD super-resolution imaging optical system[J]. Chinese Optics, 2021, 14(5): 1194-1201.
- [29] 张艺蓝, 史浩东, 王超, 等. 离轴自由曲面光学系统偏振像差特性研究[J]. 光学学报, 2021, 41(18): 190-200.  
Zhang Y L, Shi H D, Wang C, et al. Research on polarization aberration characteristics of off-axis freeform surface optical system[J]. Acta Optica Sinica, 2021, 41(18): 190-200.
- [30] Kim J, Escutti M. Demonstration of polarization grating imaging spectropolarimeter (PGIS) [J]. Proceedings of SPIE, 2010, 7672: 767208.
- [31] 王东, 颜昌翔, 张军强. 光谱偏振调制器的高精度装调方法[J]. 中国光学, 2016, 9(1): 144-154.  
Wang D, Yan C X, Zhang J Q. High accuracy alignment of spectral-polarimetric modulator[J]. Chinese Optics, 2016, 9(1): 144-154.
- [32] Craven-Jones J, Kudennov M W, Stapelbroek M G, et al. Infrared hyperspectral imaging polarimeter using birefringent prisms[J]. Applied Optics, 2011, 50(8): 1170-1185.
- [33] Gupta N. Characterization of SWIR hyperspectral imager with a multispectral polarized scene projector[J]. Proceedings of SPIE, 2013, 8707: 870706.
- [34] 朱京平, 李杰. 静态全光干涉成像光谱全偏振探测方法: CN101782433A[P]. 2010-07-21.  
Zhu J P, Li J. Static all-optical interferometric imaging spectroscopy with full polarization detection method: CN101782433A[P]. 2010-07-21.
- [35] 李杰, 朱京平. 一种轻小型干涉成像光谱全偏振探测装置: CN101793559B[P]. 2012-04-18.  
Li J, Zhu J P. A light and small interferometric imaging spectroscopy full polarization detection device: CN101793559B [P]. 2012-04-18.
- [36] Meng X, Li J X, Xu T T, et al. High throughput full Stokes Fourier transform imaging spectropolarimetry[J]. Optics Express, 2013, 21(26): 32071-32085.
- [37] Meng X, Li J X, Song H Q, et al. Full-Stokes Fourier-transform imaging spectropolarimeter using a time-division polarization modulator[J]. Applied Optics, 2014, 53(24): 5275-5282.
- [38] Reginald N L, Gopalswamy N, Yashiro S, et al. Replacing the polarizer wheel with a polarization camera to increase the temporal resolution and reduce the overall complexity of a solar coronagraph[J]. Journal of Astronomical Telescopes, Instruments, and Systems, 2017, 3(1): 014001.
- [39] 林国画, 张敏, 孟令伟, 等. 集成式偏振红外焦平面探测器的制备[J]. 激光与红外, 2019, 49(10): 1234-1238.  
Lin G H, Zhang M, Meng L W, et al. Polarizer fabricated onto infrared focal detector[J]. Laser & Infrared, 2019, 49(10): 1234-1238.
- [40] 张肃, 战俊彤, 付强, 等. 复杂海洋环境下天空光偏振特性模拟研究[J]. 光学学报, 2020, 40(22): 2201001.  
Zhang S, Zhan J T, Fu Q, et al. Simulation research on sky polarization characteristics under complicated marine environment[J]. Acta Optica Sinica, 2020, 40(22): 2201001.
- [41] Liu J, Duan J, Hao Y F, et al. Semantic-guided polarization image fusion method based on a dual-discriminator GAN[J]. Optics Express, 2022, 30(24): 43601-43621.

## Multispectral Polarization Visually Assisted Optical Imaging Technology under Harsh Conditions

Fu Qiang<sup>1\*</sup>, Zhan Junlong<sup>1</sup>, Zhang Su<sup>1</sup>, Duan Jin<sup>1</sup>, Zhu Jingping<sup>2</sup>, Huang Liqing<sup>2</sup>,  
Shi Haodong<sup>1</sup>, Li Yingchao<sup>1</sup>, Jiang Huilin<sup>1,3\*\*</sup>

<sup>1</sup>School of Optoelectronic Engineering, Changchun University of Science and Technology, Changchun 130022, Jilin, China;

<sup>2</sup>School of Telecommunication, Xi'an Jiaotong University, Xi'an 710049, Shaanxi, China;

<sup>3</sup>School of Optics and Photonics, Beijing Institute of Technology, Beijing 100081, China

### Abstract

**Objective** In view of the differences in polarization characteristics caused by different states of the detected targets, different radiation spectra, different sizes and shapes, complex transmission environment of soot and haze, and variable

light field interference, we conduct the target multispectral polarization model and polarization characteristic transmission model, develop the optimal design method of micro-nano grating polarizer array, put forward the principle and schemes of high-resolution imaging detection instruments, and propose a novel deep network to solve the polarization image fusion problem through a self-learning strategy. We aim to use multispectral polarization imaging technology to solve the problems of complex optical field interference, limited visible distance, and insufficient classification ability of optical imaging under harsh conditions.

**Methods** In this paper, the polarization imaging detection method and multispectral information fusion technology are studied, and the overall scheme of the multispectral polarization imager is proposed. Scientific methods such as the theory and model of target polarization characteristics under complex optical fields, micro-nano grid focal plane polarization device, optimization and testing of a multispectral fully polarized imaging system, and polarization image processing based on polarization difference characteristics are condensed.

Key technologies and solutions such as modeling and testing of target polarization characteristics generation and transmission, optimization of metal micro-nano grating polarization elements with high extinction ratio, the optical design of multispectral polarization imaging and testing system, and multispectral polarization information processing are analyzed. This will lay the foundation for the development of a multispectral polarization imaging detection test prototype, which will meet the practical application requirements of visual assistance and guidance in optical imaging.

**Results and Discussions** We conduct the target multispectral polarization model and polarization characteristic transmission model, which reveal typical target multispectral polarization law and haze and dusty weather multispectral polarization transmission law and provide theoretical basis for multispectral polarization information processing.

We develop the optimal design method of micro-nano grating polarizer array, solve the defects of the current defocused plane polarization imaging device that only has micro-nano linear grating and cannot produce circular polarization, and propose a new chiral micro-nano circular grating mechanism. We also analyze the physical nature of the low extinction ratio of the division of focal plane polarization imaging, put forward the physical mechanisms for the generation of the high extinction ratio of the linear grating, and discuss the effect of the deviation of the preparation parameter on the extinction ratio law. Combining the micro-nano linear grating and circular grating, we study the new device of full polarization high extinction ratio and split focal plane imaging, and lay the technical foundation for the development of multispectral and multi-dimensional polarization high-resolution imaging detection instruments.

Aiming at the problems of close detection distance, low detection sensitivity, and narrow environmental application range of the existing instruments under the haze and smoke conditions, we put forward the principle and scheme of multispectral polarization high-resolution imaging detection instruments and the design scheme of multi-optical imaging optical system for the characteristics of large loss of light energy in polarization imaging. We break through the optical system design based on the polarization aberration correction and multispectral polarization calibration, so as to significantly improve the instrument's imaging and detection ability in the haze and dusty environment.

A novel deep network is proposed to solve the polarization image fusion problem through a self-learning strategy. The network consists of an encoder layer, a fusion layer, and a decoder layer, where the feature maps extracted by the encoder are fused and then fed into the decoder to generate a fused image. Given a multidimensional polarization image, effective features are extracted from this source image, which are fused to form an information-rich polarization image for subsequent advanced image applications.

**Conclusions** Aiming at the problems of "not recognizing", "not seeing far", and "not being able to recognize" in optical detection caused by harsh environments and meteorological conditions, we put forward a multispectral polarization imaging detection technology and expect to achieve breakthroughs in three aspects: 1) in terms of device development, through the improvement of circular micro-nano grid design method and micro-nano grid substrate material-structure, it is necessary to prepare new devices with high extinction score of focal plane imaging; 2) in terms of system design, breakthroughs are required in the design of multi-optical path bias-preserving optical system, high-transmittance and high bias-preserving optical coating and other key technologies, and high spatial and temporal matching of instrument information acquisition; 3) in terms of information processing, the study of the polarization characteristic model and polarization transmission model of the target is important.

Adverse environmental and weather conditions not only have a great influence on optical imaging detection but also have an extremely serious effect on aircraft landing safety and other areas. Fog and low visibility conditions cause aircraft to fail to land properly, making flights grounded or delayed, with significant economic and social impacts. At present, to perform approach and landing under low visibility conditions, pilots mostly use ground and airborne navigation facilities/equipment to guide the aircraft to the runway in accordance with the specified flight path, mainly including instrument landing system ILS, microwave landing system MLS, satellite navigation technology GPS, laser landing system, and

visual landing system. Under extremely severe conditions such as no radar guidance or no ground indication, the aircraft cannot obtain effective and safe landing guidance and assistance through the above guidance methods. Therefore, it is of great significance to develop visual aids for aircraft landing under adverse conditions. It can improve the safety of airplane landing under bad conditions such as smoke environments, sea fog environments, and low illumination environments.

**Key words** imaging systems; multispectral polarization; visual aids; polarization characteristics; micro-nano grid